



**HAL**  
open science

## Long-term thermal ageing of the 2219-T851 and the 2050-T84 Al-Cu alloys

Nicolas Bello, Céline Larignon, Joël Douin

► **To cite this version:**

Nicolas Bello, Céline Larignon, Joël Douin. Long-term thermal ageing of the 2219-T851 and the 2050-T84 Al-Cu alloys. *Materials Today Communications*, 2021, pp.102834. 10.1016/j.mtcomm.2021.102834 . hal-03383476

**HAL Id: hal-03383476**

**<https://hal.science/hal-03383476>**

Submitted on 18 Oct 2021

**HAL** is a multi-disciplinary open access archive for the deposit and dissemination of scientific research documents, whether they are published or not. The documents may come from teaching and research institutions in France or abroad, or from public or private research centers.

L'archive ouverte pluridisciplinaire **HAL**, est destinée au dépôt et à la diffusion de documents scientifiques de niveau recherche, publiés ou non, émanant des établissements d'enseignement et de recherche français ou étrangers, des laboratoires publics ou privés.

# Long-term thermal ageing of the 2219-T851 and the 2050-T84 Al-Cu alloys

\*N. Bello<sup>1,2</sup>, C. Larignon<sup>1</sup>, and J. Douin<sup>2</sup>

<sup>1</sup>IRT Saint Exupéry

3, rue Tarfaya

31000 Toulouse, France

(\*Corresponding author: nicolas.bello@irt-saintexupery.com)

<sup>2</sup>CEMES, Université de Toulouse, CNRS

29 rue Jeanne Marvig

31055 Toulouse, France

## Abstract

In this study, the influence of high temperature exposure on mechanical properties as well as on the microstructures of two Al-Cu alloys, has been investigated. Driven by an industrial will to use structural aluminium at higher temperature than usually stated, this work is focused on the characterization of the evolution of two commercial alloys, the 2219-T851 and the 2050-T84, induced by an ageing treatment of 1000 hours at 200°C. Careful TEM observations confirm the importance of the nanoscale precipitation and that the precipitate size and distribution strongly influence the mechanical properties of the studied alloys. Results unexpectedly show that the  $\theta' - Al_2Cu$  precipitates are more stable in time than the  $T_1 - Al_2CuLi$  precipitates at this temperature. Regarding the mechanical properties related to ageing, it follows that the 2219-T851 alloy presents a reduced drop with time of its tensile test curves compared to the 2050-T84, thus a limited, and at least less pronounced, temperature dependence. For an industrial application on structural part, 2219-T851 alloy then appears to be a good candidate for long-term structural applications at intermediate temperatures.

## Keywords

Aluminium alloys, Transmission Electron Microscopy, Plasticity, ageing treatment, Mechanical Properties

## Introduction

Aerostructures manufacturers are continually seeking solutions to reduce aircraft weight, and aluminium alloys, with their low-density giving rise to excellent specific mechanical properties, often appear as a pertinent choice when metallic parts are needed. Historically developed for low-temperature applications, aluminium alloys are still being used with this specification, i.e. at temperature generally below 80°C. Some applications of aluminium alloys can be found at medium temperatures (in the range 80 – 110°C) but mainly for non-structural applications. Usually aerodynamic parts, as the wings leading edges for example, are made of aluminium alloys and the temperature can be higher than 110°C [1]. For the supersonic flight, the Concorde highest temperature was 127°C on the nose, an aerodynamic part non-essential for the aircraft structural integrity [2]. In the case of heated structural parts, titanium alloys are preferred, essentially due to their better mechanical resistance at elevated temperature. Consequently, on aircraft structures, titanium alloys are being used for in-service temperatures above 80°C and up to 400°C (with  $\alpha$ , near- $\alpha$ ,  $\beta$ , and/or near- $\beta$  structures [3,4]), while aluminium alloys are only used below 80°C-110°C for structural parts, as it is generally considered that their mechanical properties decrease excessively above 110°C. For structural applications, the replacement possibility of titanium alloys by aluminium ones for long-term use at an intermediate temperature, that is when the mechanical properties of aluminium are considered to be dropping down too rapidly, would, however, be of great interest, as such a replacement would allow weight reduction, but also cost savings through the low raw material and machinability costs. Aluminium alloys are indeed less expensive and easier machined than titanium alloys [5].

Within the framework of this project, the aim was to find an aluminium alloy with a service temperature of, at least, 150°C. To be able to use aluminium alloys at this temperature on structural aircraft parts, ageing stability must be studied. In relation with industrial purposes, the maximum service temperature has been fixed to 200°C. Hence the selection of the ageing temperature to fit this targeted in-service temperature. Following these requirements, the alloy choice has been made: two qualified aluminium alloys of the 2xxx series have been selected as the aluminium-copper alloys of this series are supposed to have a good stability after thousands of hours in temperature when compared to the other heat treatable aluminium alloys [6]. The 2219-T851 alloy was selected due to the good ageing performance [6] as well as the 2050-T84 for the results on the temperature tensile properties. As-received heat treatment was also of interest and selected to correspond to the one already used for aircraft parts and to an overaged microstructure.

Some results on the ageing of the 2xxx series aluminium alloys can be found in the literature but most of them are focused on elaboration process optimizations. Indeed, the applications of higher temperature during short periods of time, typically less than 200h [7], can enhance mechanical

properties but increase the production cost. Some recent research investigated over-ageing behaviour on Al-Cu-Li alloys between 200°C and 305°C for less than 200 hours [8,9]. However, almost no information can be found on aluminium ageing for a period as long as 500h or more. In this work, the influence of a 1000 hours thermal ageing at 200°C at room temperature tensile properties and microstructure evolution of two aluminium alloys of the 2xxx series is investigated. To follow the evolution of the studied alloys, multiscale characterization and mechanical testing have been conducted.

## Materials

The two aluminium alloys selected for this study are the 2050-T84 and the 2219-T851 alloys, with composition ranges given in Table 1. Both alloys were delivered as plate-like bulk pieces, 130 mm thick for the 2050 and 80 mm thick for the 2219. For this study, the 2050 and 2219 alloys are respectively associated with the specific thermomechanical T84 and T851 treatments. The T84 heat treatment for the AA2050 corresponds to a first solution heat treatment at  $525 \pm 5$  °C followed by a water quenching, then a cold work at approximately 4% and an artificial ageing at  $155 \pm 5$  °C for 18 hours [10,11]. The T851 heat treatment on the 2219 alloy is similar but with a solution heat treatment at  $535 \pm 5$  °C, followed by the cold working and an ageing treatment at  $175 \pm 3$  °C for 18 hours. On this last alloy, another treatment was applied: a stress relief by stretching between 1 and 3% [10]. In the following, these thermomechanical treatments are called “as-received states”.

The 2219 alloy has been developed in 1954 (year of standard designation). Some authors [12,13] have noted the high temperature stability of this alloy. They conducted several mechanical tests on a 2219-T87 alloy heat-treated between 165 and 185°C and reported stable mechanical properties of the alloy after being exposed between 12 and 30 hours at the given temperatures. The tensile yield stress value was slightly above 300 MPa and, ultimate tensile strength was around 400 MPa. Notice that these authors only studied these experimental conditions in order to improve the thermomechanical process optimization, as mentioned previously [12,13]. The 2219 alloy mostly contains  $\theta'$  –  $Al_2Cu$  precipitates, which have been widely studied in the literature [14–16]. The precipitation sequence of the  $\theta$  precipitates is now well accepted [17,18]: starting from a solid solution alloy, precipitates grow from Guinier-Preston zones to coherent  $\theta''$  precipitates to semi-coherent  $\theta'$  precipitates to incoherent  $\theta$  precipitates with the known  $Al_2Cu$  stoichiometry. The precipitation sequence can be summarized as:



Where GP stands for Guinier-Preston zones [19,20].  $\theta$ -precipitates are platelets-like precipitates lying in the  $\{001\}_{Al}$  planes with various orientation relationships with the aluminium matrix [21,22]. It is worth noting that coarser intermetallic precipitates such as T-phase  $Al_{20}Cu_2Mn_3$  are also present in the alloy microstructure [15]. These precipitates have an important influence on the corrosion sensitivity of the alloys [23], mechanical properties [1,24] and also grain size control [24,25]. They have been studied by several research teams but won't be studied here as we will focus our investigation on mechanical properties.

The 2050 alloy has been more recently developed and is part of the AIRWARE® brand developed by Alcan Rhenalu SAS (now known as Constellium®) for space and aeronautical use [26]. This alloy is the third generation of Al-Cu-Li alloys developed by Alcan Rhenalu SAS, with a reduced lithium content. This alloy's macroscopic properties and microstructure have been characterized since the early 2010s in order to understand the microstructural changes characteristic of this generation compared with the previous generation of Al-Cu-Li alloys and even with other aluminium alloy series [25,26]. Apart from  $\theta' - Al_2Cu$  precipitates, other nanometric precipitates can be found in Al-Cu-Li alloys [27]. Two types of precipitates can coexist:  $T_1 - Al_2CuLi$  and  $\delta' - Al_3Li$ .  $T_1 - Al_2CuLi$  platelet-like precipitates are lying in the  $\{111\}_{Al}$  planes. The  $T_1 - Al_2CuLi$  crystallographic structure was first determined by Meetsma et al. [14] and recently confirmed by two different research teams [28,29]. Despite their observation on previous Al-Cu-Li generations [26,30],  $\delta' - Al_3Li$  precipitates have not been found in the 2050 alloy due to the low Li content. In addition to these precipitates, and due to the alloy chemical composition, another kind of precipitate can be expected. Indeed with the presence of magnesium and silver in this alloy,  $\Omega$  precipitates can be observed [31]. These precipitates are also lying in the  $\{111\}_{Al}$  planes. Finally, as in the 2219, coarser precipitates related to heavier elements are also present in the microstructure, also affecting corrosion sensibility [32]. In this alloy, it has been found that  $Al_3Zr$  and T-phase  $Al_{20}Cu_2Mn_3$  precipitates are present [25].

## Experiments

The thermal ageing was conducted on bulk pieces placed at 200°C for 1000h under air pressure (noted 'aged' in the following). Ageing parameters have been chosen to correspond to a maximum peak temperature seen by the alloys during foreseen in-service solicitations.

To understand the alloys' behaviour before and after a long thermal ageing, several characterization methods were used: mechanical testing, optical microscopy and Scanning and Transmitting Electron Microscopy (SEM and TEM).

- Mechanical testing was performed on cylindrical specimens with an effective diameter of 6 mm in accordance with the NF EN 2002-001 standard modified using a test speed fixed at  $0.005 \text{ min}^{-1}$  (approximately  $0.8 \cdot 10^{-4} \text{ s}^{-1}$ ). The tests have been realized on a RKM250 Zwick equipment.
- Optical observations were made after etching the samples for 30 seconds with Keller's reagent. Widely used to reveal aluminium alloys microstructure, the Keller reagent is composed of 1 ml of 40 wt.% HF, 1.5 ml of 35 wt.% HCl, 2.5 ml of 68 wt.% HNO<sub>3</sub> and 95 ml of H<sub>2</sub>O [33].
- Scanning Electron Microscopy observations were performed using a dual-beam FEI Helios 600 Nanolab. SEM samples were smoothed out with graduated SiC papers and finally polished with a 1 µm suspended diamond solution. The samples were observed with a 20 kV acceleration tension and a current of 1.4 nA. A circular backscatter (CBS) detector was used to highlight the presence of intermetallic precipitates. To complete the study, size characterization of the coarse precipitates was conducted by Image J software ([imagej.nih.gov/ij/](http://imagej.nih.gov/ij/)) on SEM-CBS images.
- Transmission Electron Microscopy observations were conducted on a JEOL JEM2010 HC (with an LaB6 filament) at 200 kV. Microstructure characterization was carried out on thin foils prepared by twin-jet electro-polishing in a 2/3 vol. % Methanol and 1/3 vol. % Nitric Acid solution at 20 V and -15°C on samples mechanically polished until reaching a thickness of 200 µm. Square samples (approximately 2 x 2 mm<sup>2</sup>) glued with silver lacquer to a copper grid were prepared for classical TEM imaging.

All observations were made on the as-received state alloys and after the long thermal ageing.

## Mechanical properties

Tensile tests were realized at room temperature with the parameters given above on the as-received and aged alloys (Figure 1). The values of yield and ultimate tensile strengths (referred in the following as YS and US) are reported in table 2.

First of all, for alloys in the as-received state, the measured stress-strain curves are in a good agreement with what was expected from the patent presented by Alcan in 2010 [34] or by Chemin *et al.* [35] for 2050-T84 and reported in previous works for 2219 alloy [10]. The 2050-T84 alloy has a high yield tensile strength, comparable to the alloys of the 7xxx series, and significantly higher than that of 2219, with equivalent ductility. As expected, after being submitted to a long-term ageing process, yield and ultimate tensile stresses of both alloys are significantly reduced. The most affected material by long-term ageing is the 2050 alloy for which the decrease of static yield tensile strength (YS) is estimated to 208 MPa in the Rolling Direction (RD), that is a reduction of about 40% from the value before ageing. The impact of ageing on the 2219 alloy is less pronounced with a reduction limited to 79 MPa in the RD, that is about 17%. The evolution of YS with thermal ageing is also more significant for the 2050 alloys with a 271 MPa (54%) drop than for the 2219 alloy (106 MPa, i.e. a reduction of 30% in the RD). The 2219 alloy then appears with slightly better capabilities than the 2050 after ageing. Clearly speaking, while the 2050 alloy shows a better tensile resistance than the 2219 alloy in the as-received condition, the 2219 alloy is better than the 2050 after ageing treatment. As this heat treatment could be abruptly correlated to real conditions of use, this may have profound industrial implications.

Another important point to emphasize is the differences in the stress-strain curve shapes, which can be clearly evidenced by plotting the Kocks-Mecking curves (work hardening rates  $\partial\sigma/\partial\varepsilon$  as a function of reduced stress (Figure 1b)) [36,37]. Heat treatment does not have a significant impact on the hardening rate of the 2219 alloy. On the contrary, there is a great change for the 2050 alloy before and after heat treatment. Between 1% and 3% of deformation, that is when the deformation process has reached a steady-state behaviour, the hardening rate of the as-received 2050 alloy is significantly lower than the ones for the aged 2050, whose behaviour looks like the one of the 2219 alloys, thus indicating a change in the involved deformation mechanisms.

Two hypotheses can be put forward to explain this change. Firstly, it could result from the elaboration process. Indeed, the 2219 alloy underwent a stress relief treatment by stretching, and not the 2050 alloy. On a general point of view, a higher initial dislocation density would result in an improved initial yield stress, essentially related to forest hardening, and consequently a lower hardening rate. However, it is not believed that a different initial dislocation density would modify the shape of the work-hardening rate curve.

Secondly, it is well known, and it has been observed in aluminium alloys [38,39], that the hardening rate is very dependent upon the fine microstructure of the alloys. Indeed, the study of the influence of the size and shape of the precipitates on the hardening response indicates that smaller and more shearable precipitates are generally ascribed to a lower hardening rate than larger ones, which are bypassed during deformation through the Orowan process. A change of the strain-stress curve has already been observed for overaged Al-Cu-Li alloys [8,38,39]. In an Al-Cu-Li alloy, the authors observed a low hardening rate with the presence of small  $T_1$  precipitates while a high-hardening rate for thicker  $T_1$  precipitates. The difference between the two behaviours has been linked to the dislocations/precipitate interaction nature: shearing or bypassing, respectively [38,39].

It is then important to realize that the evolution of the shape of the strain-stress curves clearly indicates a modification of the microstructural mechanisms activated during the deformation in the 2050 alloy between the as-received state and the thermally aged state, while for the 2219 alloy, only a few, if any, microstructural changes should be expected.

## Microstructure description

Alloys have been first observed at a medium scale using Optical and Scanning Electron Microscopes (SEM), with the main objectives to measure the grains sizes and to identify the relevant microstructural features.

The grain sizes were measured using the intercept method on optical micrographs. Straight lines were drawn on the three characteristic directions, Rolling Direction (RD), Transversal Direction (TD) and Short Direction (SD), relative to the hot-rolling directions of the plates, to determine the mean intercept value and then the mean grains length and width. Average grain size and related form factors are reported in Table 3. In the following, only the dimension of grains observed on the TD-SD plane, that is perpendicular to the rolling direction, are reported. Notice that due to the frequent observations of sub-grain boundaries in the 2050 alloy and in order to confirm the presence of sub-grains boundaries in this alloy, EBSD SEM technique has been used. Since this technique was only employed to discriminate the grain boundary nature, the results are not presented here.

For the 2219 alloy (Figure 2) in the as-received state, the mean grain dimension is approximately 290  $\mu\text{m}$  with a form factor of 1.84 (Table 3). Similar values have already been reported in the literature [13]. On the as-received 2050 alloy, the grain dimensions are smaller. The mean grain dimension is approximately 120  $\mu\text{m}$  with a form factor of 1.5. The etching initially performed to allow a better observation of the grain boundaries also revealed a precipitate free zone (PFZ) near the grain boundaries in the 2050 alloy (Figure 3a.). This precipitate free zone can be evidenced using SEM-CBS. On the Figure 3a. and in the proximity of a grain boundary, noted A for example, it is possible to observe less white signal compared with the grain centre. As the Keller reactant is sensitive to the hardening precipitates present in the aluminium matrix, this would tend to indicate that, in the 2050 alloy, diffusion is accelerated in the vicinity of grain boundaries, preventing precipitation from occurring or promoting the dissolution of close precipitates. Such PFZ has also been observed elsewhere [32].

In order to confirm the nature of the coarse precipitates present in both 2219 and 2050 alloy microstructures, SEM-EDX analysis and image analysis have been conducted. On the 2219 alloy, results confirmed the large presence of coarse precipitates of Al-Cu within the microstructure. In order to discriminate the nature of the analysed precipitates, surface density measurements have been made. The quantification made with ImageJ software indicates the presence of Al-Cu precipitates larger than 7,5  $\mu\text{m}^2$ . Other smaller precipitates, less than 7,5  $\mu\text{m}^2$ , are present and are mostly composed by Al-Cu-Mn-Fe. For the 2050 alloy, fewer precipitates can be observed. The larger ones, bigger than 7,5  $\mu\text{m}^2$ , are Al-Cu-Mn-Fe precipitates while the smaller ones, less than 7,5  $\mu\text{m}^2$  are Al-Ti-Mg-Mn precipitates. The analysis of the precipitate surface measured by image

analysis emphasize the difference between the two alloys, where in the 2219 alloy, the precipitates have a measured surface density of 2,39%, compared to the 0.99% measured in the 2050 alloy.

For both alloys, the ageing treatment does not induce drastic changes in the mean grain size (Table 3). With the SEM observations and for the 2050 alloy, the ageing treatment results in an increased precipitation in grains and sub-grain boundaries. In addition, the precipitate free zone along the grain boundaries is still present (Figure 3). On the microstructure of the 2219 alloy, no significant change can be identified at this scale of observation.

The modification induced by the ageing treatment on the tensile properties observed previously in both alloys might have been related to the Hall-Petch effect via a grain size modification. In this case, this effect cannot be addressed:

- The microstructure of the 2050 alloy is not stable throughout the ageing treatment,
- The introduction of deformation during the elaboration processes of the two alloys,
- The absence of significant change on the 2219 alloy microstructure explaining the tensile property variations.

With these points, the observed increase of this mechanical property cannot be ascribed to grain size variation. It is believed that the origin of these modifications requires a study at a finer scale, with TEM observations.

## Evolution of the Fine Scale Microstructure

Conventional TEM observations clearly show that the microstructure of both as-received alloys is already filled with numerous hardening (nano)precipitates (Figure 4). These fine precipitates are known to impede the motion of dislocations upon stress, thus giving rise to a substantial increase in yield stress compared to pure aluminium [6].

In both alloys, these hardening precipitates are plate-like shaped. In the 2050-T84 alloy (Figure 4a.), the precipitates can be indexed using Selected Area Electron Diffraction (SAED, Figure 5a.) pattern as  $T_1 - Al_2CuLi$  precipitates. Figure 6 has been used for the SAED indexation, as it presents the diffraction pattern of the precipitates found in 2219 and 2050 alloys when orientated in a  $\langle 001 \rangle_{Al}$  direction. These precipitates have been previously reported in this alloy [26] as well as in other Al-Cu-Li alloys, such as in 2198 [39] or 2055 alloy [8]. They have been widely studied in the literature of Al-Cu-Li alloys, and, as observed here, are known to form platelets lying in the  $\{111\}_{Al}$  planes of the aluminium matrix: this is why they appear edge-on in the  $\langle 110 \rangle_{Al}$  observation directions (Figure 4a.). During deformation, these 3 atomic layers wide precipitates [29,38] are usually sheared by gliding dislocations. It is worth emphasizing that while these precipitates have a small thickness, their density here is inversely very high. This has a direct consequence on the mechanical properties of the 2050 alloy: as the efficiency of the precipitates to block the dislocations is a function of the distance between precipitates, a high density of precipitates well explains the high level of yield stress observed for this alloy. The overlapping of stress fields surrounding the precipitates has an experimental drawback: the difficulty to observe well resolved contrasts in conventional TEM.

Compared to the microstructure of the as-received 2050 alloy observed by TEM, the as-received 2219 one (Figure 4b.) contains different larger precipitates. The plate-like precipitates observed in this alloy microstructure are  $\theta' - Al_2Cu$  precipitates lying in the  $\{100\}_{Al}$  planes. This is why they appear edge-on with a  $90^\circ$  symmetry when observed along a  $\langle 001 \rangle_{Al}$  direction (Figure 4b.) Even though the exact structure is still being discussed, the observed SAED pattern (Figure 5b.) matches with the precipitate structure proposed by [22]. Due to their larger size, these precipitates are more difficult to shear and then mostly bypassed by the Orowan mechanism [15]. Between these thicker precipitates, smaller precipitates can also be observed, areas are pointed with the C arrow (Figure 4b.). To confirm the nature of these precipitates, the selection of a small area to have a representative SAED pattern is experimentally very difficult. Nevertheless, considering the precipitate orientation and the alloy chemistry, it is possible to assume that these are  $\theta''$  or  $\theta'$  precipitates as the GP zones are nearly impossible to observe with conventional TEM. These smaller precipitates play an important role in the as-received alloy, as they decrease the mean spacing value between precipitates and thus contribute to the enhanced mechanical properties.

After the 1000h ageing treatment at 200°C, the fine microstructure of both alloys has changed (Figure 7). In the 2050 microstructure (Figure 7a.),  $T_1 - Al_2CuLi$  precipitates can still be observed but they appear thicker compared to the as-received alloy, precipitates pointed by B arrows (Figure 7a.). Also, a new precipitate family can be observed, the precipitates are indicating with A arrows on Figure 7a. Using SAED, this new precipitate family can also be indexed as  $\theta' - Al_2Cu$  precipitates. Figure 7a. presents the SAED pattern orientated in a  $\langle 001 \rangle_{Al}$  direction show strikes with thicker parts where the diffraction of the  $\theta'$  phase occur [40]. Due to the crystal orientation  $\langle 110 \rangle_{Al}$ , they are not being seen edge-on as they are lying in the  $\{100\}_{Al}$  planes. Thus, they appear thicker than the  $T_1$  precipitates in the Figure 7a. Notice that it is not possible to know if these precipitates, as well as some precursors such as GPI zones or GPII zones/ $\theta''$  precipitates, appear during the ageing treatment or if they were too small to be seen by conventional TEM. In fact, streaking along the  $\langle 100 \rangle_{Al}$  directions which can be observed on the SAED pattern of the as-received 2050-T84 (Figure 5b.) is known to be due to the presence of Cu-rich GP zones in the  $\{100\}_{Al}$  planes [41]. With further ageing, the streaking presents brighter points near the diffraction of the  $\theta'$  phase.

From this observation, it results that the density of hardening precipitates has largely felt down after ageing of the 2050 alloy, resulting in a consequent increase in the mean distance between precipitates, thus lowering the yield stress by promoting Orowan process instead of shearing of precipitates. This is fully in accordance with the reduction of the yield stress, and the variation of the work-hardening rate (Figure 1b.), which is low for as-received, thus connected with shearing of precipitates, and higher after ageing, thus related to more frequent Orowan mechanism [15]. This can explain the wide presence of  $T_1$  precipitates in the as-received 2050 alloy.

As mentioned before,  $\Omega$  precipitates have been reported in the 2050 alloy. However, as noted by different authors, the SAED pattern of the  $\Omega$  and of the  $T_1$  phases are too close to be distinguished. For example, SAED pattern of an Al-Cu-Li without magnesium or silver [42] is very close to an SAED pattern of an Al-Cu-Mg-Mn-Ag alloy [41]. The  $\Omega$  precipitates have not been found in Al-Cu-Li alloys so far, and in a recent study highlighting the effect of magnesium in these alloys, it has been concluded that magnesium allows a selective precipitation of the  $T_1 - Al_2CuLi$  precipitates [43].

On the 2219 alloy, the  $\theta' - Al_2Cu$  precipitates are also thicker after the ageing treatment. This is also confirmed by the SAED pattern observations. The Figure 7b. which corresponds to the diffraction of the 2219 aged microstructure, is quite similar to the Figure 5b., the as-received one. However, and even if it appears that the small-sized precipitates have disappeared or at least became very small and by consequence hardly visible, the important point is that there is not a drastic change of the mean distance between  $\theta' - Al_2Cu$  precipitates before and after ageing. It thus results that the yield stress of the 2219 alloy after ageing, while reduced compared to as-received alloy, has essentially retained its magnitude or only slightly decreased. Regarding the

hardening rate, as the mechanism by which dislocations overcome the precipitates is also essentially conserved, it is not abnormal to observe equivalent hardening rates before and after ageing for the 2219 alloy.

It is worth emphasizing that a detailed statistical description of the distances between precipitates, correlated with the nature of the dislocation/precipitate interaction, would allow estimating the theoretical yield strengths, to be compared with the measured ones (work in progress).

At this point, the precipitates stability can be discussed. The presented results have shown, for the ageing behavior of the 2020-T84 alloy, the precipitation of the  $\theta'$  phase. This phase appears with the ageing treatment, sign of the thermal stability at this temperature when compared to the  $T_1$  phase. First, the precipitation temperature can be addressed. These two phases present very close precipitation temperature: from 280°C to 300°C at 5°C.min<sup>-1</sup> [44–46] for the  $\theta'$  phase and 280°C and 325°C at 50°C.min<sup>-1</sup> [39] for the  $T_1$  phase. Due to the heating rate variation, the precipitation temperature of the  $T_1$  phase is lower than the presented values when the heating rate is 5°C.min<sup>-1</sup>. Thus,  $T_1$  phase exists at lower temperature than  $\theta'$  phase. Secondly, the growth mechanism can be addressed. It is believed that after approximately 80 hours at 190°C, the growth of the  $T_1$  phase has stopped with a mean thickness of 2 nm [39]. For the  $\theta'$  phase, platelets have been measured up to approximately 14 nm ( $24 c_{\theta'}$  with  $c_{\theta'} = 5.80 \text{ \AA}$  [22]) after 24 hours placed at 200°C. Due to the close precipitation temperatures and growth possibility of the  $\theta'$  and  $T_1$  phases, the apparition of the  $\theta'$  during the ageing treatment at 200°C indicates its stability when compared to the  $T_1$  phase.

## Conclusions

In order to consider the use of aluminium alloys at an intermediate temperature for a structural application, mechanical test followed by the characterization of the microstructural evolution has been conducted on two 2xxx aluminium alloys, in the as-received T8 state and after a supplementary ageing treatment of 1000 hours at 200°C. The results have shown a drop of tensile properties of both alloys but with very different magnitudes. After the ageing treatment, the 2219 yield stress only drops of about 80 MPa while the 2050 yield stress drops of more than 200 MPa (tests performed in the rolling direction). This work demonstrates that these changes are linked with the evolution of the microstructure at a fine scale. Indeed, 2219 alloy presents only a slight change in size and distribution of the hardening nanoprecipitation. For the 2050 alloy, the disappearance of the smallest precipitates, which were responsible for the superior mechanical properties in the as-received state, is at the origin of its great strength decay. It is then envisioned that when the mechanical properties stability with temperature is sought, microstructures with more stable precipitates, such as the  $\theta'$  -  $Al_2Cu$  ones, should be favoured, compared to  $T_1$  -  $Al_2CuLi$  precipitates giving rise to better mechanical properties but less stable in time with temperature.

## References

- [1] P. Chen, The effects of heat treatment on the microstructure and mechanical properties of the AA2618 DC cast plate, 2012. <https://doi.org/10.1073/pnas.0703993104>.
- [2] Accelerated Aging of Materials and Structures, National Academies Press, Washington, D.C., 1996. <https://doi.org/10.17226/9251>.
- [3] M. Peters, J. Kumpfert, C.H. Ward, C. Leyens, Titanium alloys for aerospace applications, *Advanced Engineering Materials*. 5 (2003) 419–427. <https://doi.org/10.1002/adem.200310095>.
- [4] R.R. Boyer, An overview on the use of titanium in the aerospace industry, *Materials Science and Engineering A*. 213 (1996) 103–114. [https://doi.org/10.1016/0921-5093\(96\)10233-1](https://doi.org/10.1016/0921-5093(96)10233-1).
- [5] S.A. Niknam, R. Khettabi, V. Songmene, Machinability and Machining of Titanium Alloys: A Review, in: 2014: pp. 1–30. [https://doi.org/10.1007/978-3-662-43902-9\\_1](https://doi.org/10.1007/978-3-662-43902-9_1).
- [6] R. Develay, Aluminium et alliages d'aluminium corroyés : propriétés métalliques Aluminium et alliages d'aluminium corroyés : propriétés métalliques, *Techniques de l'Ingenieur*. 33 (1992).
- [7] L. Ceschini, A. Morri, A. Morri, M. Di Sabatino, Effect of thermal exposure on the residual hardness and tensile properties of the EN AW-2618A piston alloy, *Materials Science and Engineering: A*. 639 (2015) 288–297. <https://doi.org/http://dx.doi.org/10.1016/j.msea.2015.04.080>.
- [8] E. Balducci, L. Ceschini, S. Messieri, S. Wenner, R. Holmestad, Effects of overaging on microstructure and tensile properties of the 2055 Al-Cu-Li-Ag alloy, *Materials Science & Engineering A*. 707 (2017) 221–231. <https://doi.org//10.1016/j.msea.2017.09.051>.
- [9] E. Balducci, L. Ceschini, S. Messieri, S. Wenner, R. Holmestad, Thermal stability of the lightweight 2099 Al-Cu-Li alloy: Tensile tests and microstructural investigations after overaging, *Materials & Design*. 119 (2017) 54–64. <https://doi.org/10.1016/j.matdes.2017.01.058>.
- [10] J.G. Kaufman, Understanding the Aluminum Temper Designation System, 2000. <https://doi.org/10.1361/iaat2000p039>.
- [11] A. Danielou, C. Gasqueres, C. Sigli, T. Warner, Aluminium-copper-lithium alloy having improved mechanical strength and improved toughness, 2010.
- [12] R.K. Gupta, R. Panda, A.K. Mukhopadhyay, V.A. Kumar, P. Sankaravelayutham, K.M. George, Study of Aluminum Alloy AA2219 After Heat Treatment, *Metal Science and Heat Treatment*. 57 (2015) 350–353. <https://doi.org/10.1007/s11041-015-9888-0>.
- [13] P. Naga Raju, K. Srinivasa Rao, G.M. Reddy, M. Kamaraj, K. Prasad Rao, Microstructure and high temperature stability of age hardenable AA2219 aluminium alloy modified by Sc, Mg and Zr additions, *Materials Science and Engineering A*. 464 (2007) 192–201. <https://doi.org/10.1016/j.msea.2007.01.144>.

- [14] A. Meetsma, J.L. De Boer, S. Van Smaalen, Refinement of the crystal structure of tetragonal Al<sub>2</sub>Cu, *Journal of Solid State Chemistry*. 83 (1989) 370–372. [https://doi.org/10.1016/0022-4596\(89\)90188-6](https://doi.org/10.1016/0022-4596(89)90188-6).
- [15] J. Da Costa Teixeira, L. Bourgeois, C.W. Sinclair, C.R. Hutchinson, The effect of shear-resistant, plate-shaped precipitates on the work hardening of Al alloys: Towards a prediction of the strength-elongation correlation, *Acta Materialia*. 57 (2009) 6075–6089. <https://doi.org/10.1016/j.actamat.2009.08.034>.
- [16] X.Q. Zhao, M.J. Shi, J.H. Chen, S.B. Wang, C.H. Liu, C.L. Wu, A facile electron microscopy method for measuring precipitate volume fractions in AlCuMg alloys, *Materials Characterization*. 69 (2012) 31–36. <https://doi.org/10.1016/j.matchar.2012.04.009>.
- [17] Y.C. Lin, Y.C. Xia, Y.Q. Jiang, H.M. Zhou, L.T. Li, Precipitation hardening of 2024-T3 aluminum alloy during creep aging, *Materials Science and Engineering A*. 565 (2013) 420–429. <https://doi.org/10.1016/j.msea.2012.12.058>.
- [18] Z. Shen, Q. Ding, C. Liu, J. Wang, H. Tian, J. Li, Z. Zhang, Atomic-scale mechanism of the  $\theta'' \rightarrow \theta'$  phase transformation in Al-Cu alloys, *Journal of Materials Science and Technology*. 33 (2017) 1159–1164. <https://doi.org/10.1016/j.jmst.2016.08.031>.
- [19] A. Guinier, Structure of Age-Hardened Aluminium-Copper Alloys, *Nature*. 142 (1938) 569–570. <https://doi.org/10.1038/142569b0>.
- [20] G.D. Preston, Structure of Age-Hardened Aluminium-Copper Alloys, *Nature*. 142 (1938) 570–570. <https://doi.org/10.1038/142570a0>.
- [21] B. Noble, Theta-prime precipitation in aluminium-copper-cadmium alloys, *Acta Metallurgica*. 16 (1968) 393–401. [https://doi.org/10.1016/0001-6160\(68\)90026-6](https://doi.org/10.1016/0001-6160(68)90026-6).
- [22] L. Bourgeois, C. Dwyer, M. Weyland, J.-F. Nie, B.C. Muddle, Structure and energetics of the coherent interface between the  $\theta'$  precipitate phase and aluminium in Al–Cu, *Acta Materialia*. 59 (2011) 7043–7050. <https://doi.org/10.1016/j.actamat.2011.07.059>.
- [23] R. Grilli, M.A. Baker, J.E. Castle, B. Dunn, J.F. Watts, Localized corrosion of a 2219 aluminium alloy exposed to a 3.5% NaCl solution, *Corrosion Science*. 52 (2010) 2855–2866. <https://doi.org/10.1016/j.corsci.2010.04.035>.
- [24] F. Liu, Z. Liu, P. Jia, Effect of T-phase on microstructure of the hot rolled Al–Cu–Mg alloy, *Journal of Alloys and Compounds*. 825 (2020) 154190. <https://doi.org/10.1016/j.jallcom.2020.154190>.
- [25] R.J. Rioja, J. Liu, The evolution of Al-Li base products for aerospace and space applications, *Metallurgical and Materials Transactions A: Physical Metallurgy and Materials Science*. 43 (2012) 3325–3337. <https://doi.org/10.1007/s11661-012-1155-z>.
- [26] P. Lequeu, K.P. Smith, A. Daniélou, Aluminum-copper-lithium alloy 2050 developed for medium to thick plate, *Journal of Materials Engineering and Performance*. 19 (2010) 841–847. <https://doi.org/10.1007/s11665-009-9554-z>.

- [27] J. Han, Z. Zhu, H. Li, C. Gao, Microstructural evolution, mechanical property and thermal stability of Al–Li 2198-T8 alloy processed by high pressure torsion, *Materials Science and Engineering: A*. 651 (2016) 435–441. <https://doi.org/10.1016/j.msea.2015.10.112>.
- [28] C. Dwyer, M. Weyland, L.Y. Chang, B.C. Muddle, Combined electron beam imaging and ab initio modeling of T1 precipitates in Al–Li–Cu alloys, *Applied Physics Letters*. 98 (2011) 201909. <https://doi.org/10.1063/1.3590171>.
- [29] P. Donnadiou, Y. Shao, F. De Geuser, G.A. Botton, S. Lazar, M. Cheynet, M. de Boissieu, A. Deschamps, Atomic structure of T1 precipitates in Al–Li–Cu alloys revisited with HAADF-STEM imaging and small-angle X-ray scattering, *Acta Materialia*. 59 (2011) 462–472. <https://doi.org/10.1016/j.actamat.2010.09.044>.
- [30] A. Williams, *Microstructural Analysis of Aluminium Alloy 2096 as a Function of Heat Treatment* By, 2010.
- [31] B.C. Muddle, I.J. Polmear, The precipitate  $\Omega$  phase in Al-Cu-Mg-Ag alloys, *Acta Metallurgica*. 37 (1989) 777–789. [https://doi.org/10.1016/0001-6160\(89\)90005-9](https://doi.org/10.1016/0001-6160(89)90005-9).
- [32] V. Proton, J. Alexis, E. Andrieu, J.Ô. Delfosse, A. Deschamps, F. De Geuser, M.C. Lafont, C. Blanc, The influence of artificial ageing on the corrosion behaviour of a 2050 aluminium-copper-lithium alloy, *Corrosion Science*. 80 (2014) 494–502. <https://doi.org/10.1016/j.corsci.2013.11.060>.
- [33] E.H.Jr. Dix, F. Keller, Keller's reagent, *Mining and Metallurgy*. 9 (1929).
- [34] T. Warner, C. Sigli, C. Gasqueres, A. Danielou, *Aluminum-Copper-Lithium Alloy With Improved Mechanical Strength and Toughness*, US20110209801 A2, 2011.
- [35] A.E.A. Chemin, C.M. Afonso, F.A. Pascoal, C.I. dos S. Maciel, C.O.F.T. Ruchert, W.W. Bose Filho, Characterization of phases, tensile properties, and fracture toughness in aircraft-grade aluminum alloys, *Material Design & Processing Communications*. 1 (2019) 1–13. <https://doi.org/10.1002/mdp2.79>.
- [36] U.F. Kocks, H. Mecking, Physics and phenomenology of strain hardening: the FCC case, *Progress in Materials Science*. 48 (2003) 171–273. [https://doi.org/10.1016/S0079-6425\(02\)00003-8](https://doi.org/10.1016/S0079-6425(02)00003-8).
- [37] U.F. Kocks, Laws for Work-Hardening and Low-Temperature Creep, *Journal of Engineering Materials and Technology*. 98 (1976) 76–85. <https://doi.org/10.1115/1.3443340>.
- [38] A. Deschamps, B. Decreus, F. De Geuser, T. Dorin, M. Weyland, The influence of precipitation on plastic deformation of Al-Cu-Li alloys, *Acta Materialia*. 61 (2013) 4010–4021. <https://doi.org/10.1016/j.actamat.2013.03.015>.
- [39] T. Dorin, F. de Geuser, W. Lefebvre, C. Sigli, A. Deschamps, Strengthening mechanisms of T1 precipitates and their influence on the plasticity of an Al-Cu-Li alloy, *Materials Science and Engineering A*. 605 (2014) 119–126. <https://doi.org/10.1016/j.msea.2014.03.024>.

- [40] S. Li, J. Zhang, J. Yang, Y. Deng, X. Zhang, Influence of Mg Contents on Aging Precipitation Behavior of Al–3.5Cu–xMg Alloy, *Acta Metallurgica Sinica (English Letters)*. 27 (2014) 107–114. <https://doi.org/10.1007/s40195-014-0033-7>.
- [41] A.K. Mukhopadhyay, G. Eggeler, B. Skrotzki, Nucleation of  $\Omega$  phase in an Al-Cu-Mg-Mn-Ag alloy aged at temperatures below 200°C, *Scripta Materialia*. 44 (2001) 545–551. [https://doi.org/10.1016/S1359-6462\(00\)00650-3](https://doi.org/10.1016/S1359-6462(00)00650-3).
- [42] R. Yoshimura, T.J. Konno, E. Abe, K. Hiraga, Transmission electron microscopy study of the evolution of precipitates in aged Al–Li–Cu alloys: the  $\theta'$  and T1 phases, *Acta Materialia*. 51 (2003) 4251–4266. [https://doi.org/10.1016/S1359-6454\(03\)00253-2](https://doi.org/10.1016/S1359-6454(03)00253-2).
- [43] E. Gumbmann, W. Lefebvre, F. De Geuser, C. Sigli, A. Deschamps, The effect of minor solute additions on the precipitation path of an Al-Cu-Li alloy, *Acta Materialia*. 115 (2016) 104–114. <https://doi.org/10.1016/j.actamat.2016.05.050>.
- [44] M. Härtel, S. Wagner, P. Frint, M.F.X. Wagner, Effects of particle reinforcement and ECAP on the precipitation kinetics of an Al-Cu alloy, *IOP Conference Series: Materials Science and Engineering*. 63 (2014). <https://doi.org/10.1088/1757-899X/63/1/012080>.
- [45] P. Bassani, E. Gariboldi, D. Ripamonti, Thermal analysis of Al-Cu-Mg-Si alloy with Ag/Zr additions, *Journal of Thermal Analysis and Calorimetry*. 91 (2008) 29–35. <https://doi.org/10.1007/s10973-007-8376-1>.
- [46] I.N. a. Oguocha, S. Yannacopoulos, Precipitation and dissolution kinetics in Al–Cu–Mg–Fe–Ni alloy 2618 and Al–alumina particle metal matrix composite, *Materials Science and Engineering: A*. 231 (1997) 25–33. [https://doi.org/10.1016/S0921-5093\(97\)00065-8](https://doi.org/10.1016/S0921-5093(97)00065-8).
- [47] A. Deschamps, M. Garcia, J. Chevy, B. Davo, F. de Geuser, Influence of Mg and Li content on the microstructure evolution of Al[ $\text{Cu}$ ]Li alloys during long-term ageing, *Acta Materialia*. 122 (2017) 32–46. <https://doi.org/10.1016/j.actamat.2016.09.036>.
- [48] N. Bello, Effets d'un vieillissement longue durée sur deux alliages d'aluminium de la série 2000, Thèse de doctorat de l'Université Fédérale de Toulouse, 2018.

Table 1. Nominal composition of the studied 2219 and 2050, as per AMS4262 and AMS4413 respectively.

Alloy	Constituents (wt.%)										
	Cu	Fe	Mg	Mn	Si	Ti	V	Zn	Zr	Li	Ag
2219	5.80–6.80	<0.30	0.02	0.20–0.40	<0.20	0.02–0.10	0.05–0.15	<0.10	0.10–0.25	-	-
2050	3.20–3.90	0.1	0.20–0.60	0.20–0.50	0.08	-	-	0.25	0.06–0.14	0.70–1.30	0.29

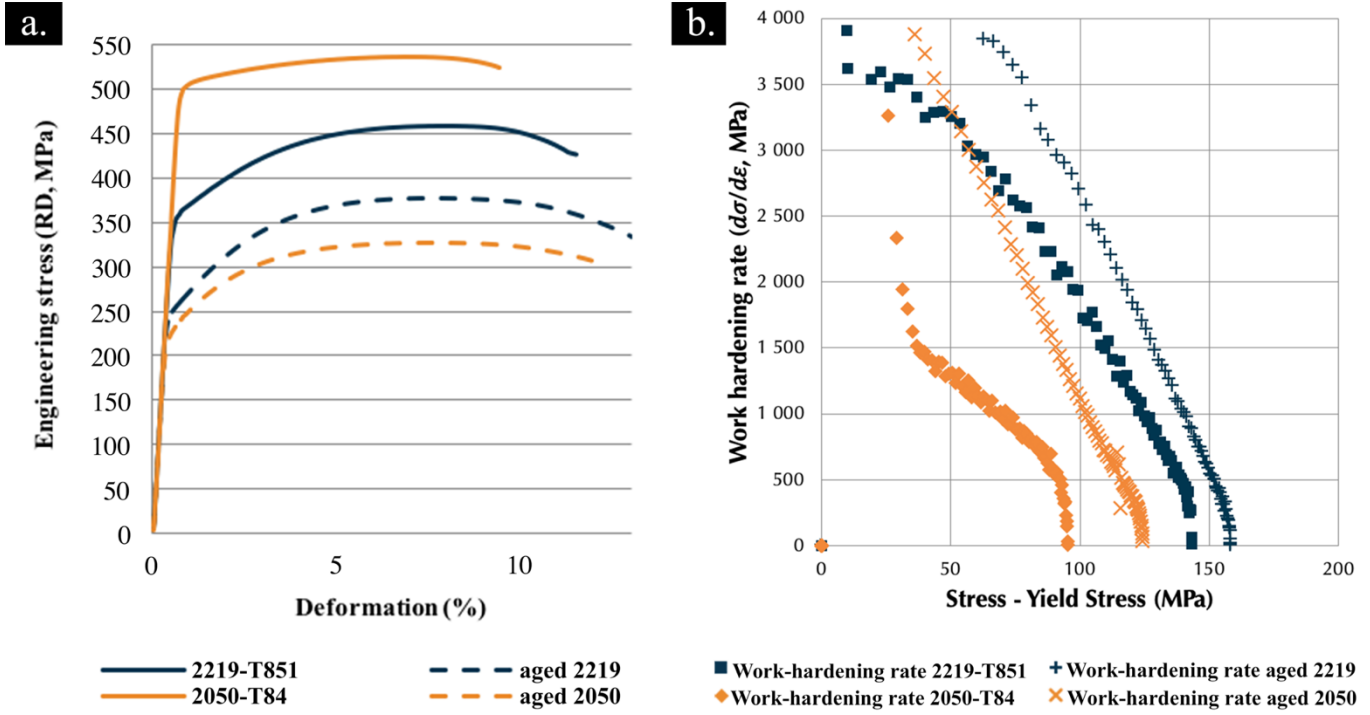


Figure 1. a. Engineering stress-strain tensile tests performed at room temperature and b) the corresponding work-hardening rates (in a log-log scale).

Table 2. Summary of the tensile tests realized at room temperature for the as-received alloys and Thermal Aged alloys (noted 'aged') (Yield Tensile Strength (YS) and ultimate (US) strength values and the elongation ( $\varepsilon$ ) at breaking are reported in the Rolling Direction (RD) and the Transverse Direction (TD) of the plates).

Alloy	2050		2219	
Heat treatment	T84	aged	T851	aged
Ftu (MPa)				
RD	535 ± 2	327 ± 3	457 ± 2	378 ± 5
TD	517 ± 4	330 ± 2	431 ± 7	373 ± 5
Fty (MPa)				
RD	502 ± 2	231 ± 3	358 ± 1	252 ± 3
TD	463 ± 3	231 ± 2	350 ± 5	245 ± 3
$\varepsilon$ (%)				
RD	9.7 ± 0.8	12.4 ± 0.7	11.2 ± 0.4	13.4 ± 0.4
TD	7.4 ± 0.9	10.0 ± 0.6	8.0 ± 0.3	9.8 ± 0.4

Table 3. Grains dimensions and aspect ratio of the 2050 and 2219 alloys in as-received states (T84 and T851) and after the Thermal Ageing (TA1). Results are given for Rolling Direction (RD), Transverse Direction (TD) and Short Direction (SD).

Alloy	2050		2219	
Heat treatment	T84	TA1	T851	TA1
Measured dimension				
RD, $\mu\text{m}$	127 ± 13	132 ± 35	299 ± 32	234 ± 29
Aspect ratio				
RD-TD	1.6	2.3	1.9	1.8
RD-SD	3.2	4.0	4.0	3.4
TD-SD	2.0	1.8	2.2	1.9

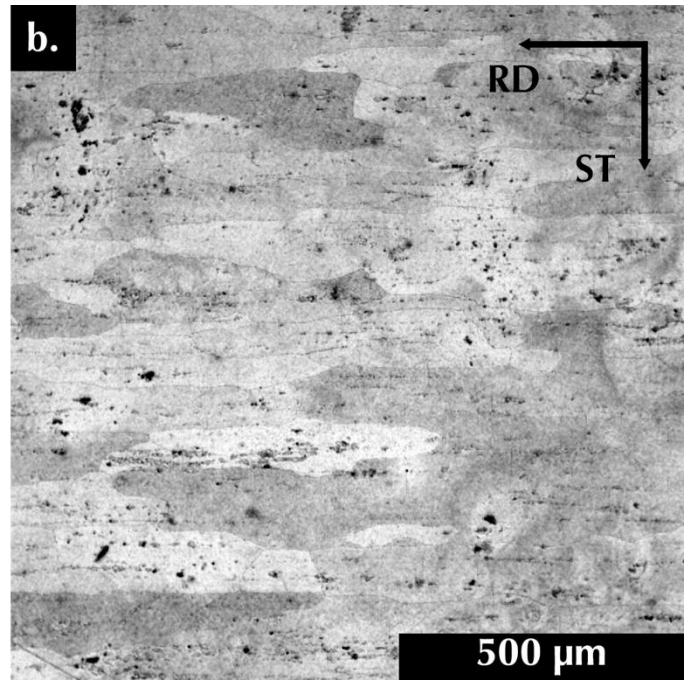
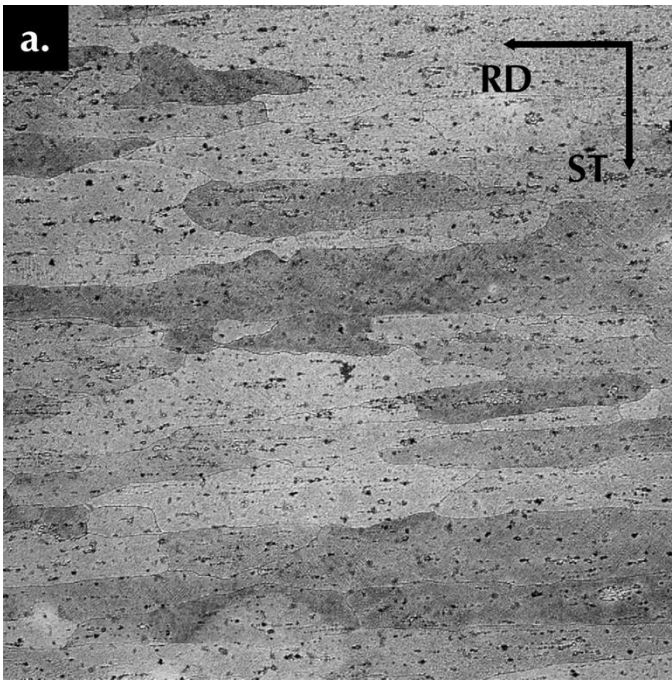


Figure 2. Optical micrographs of the 2219 alloy a. as-received state and b. after ageing. Rolling direction and short transverse directions are noted on the micrographs RD and ST respectively. Dark dots are related to the presence of coarse precipitates.

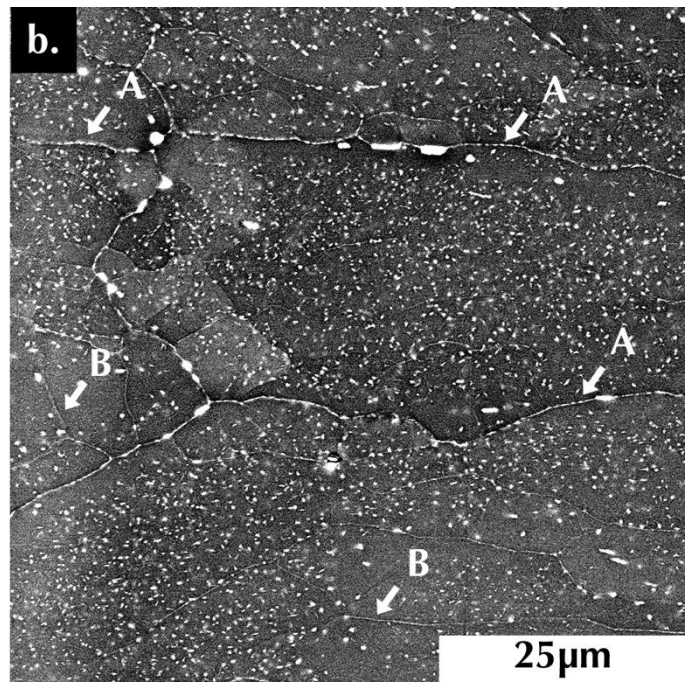
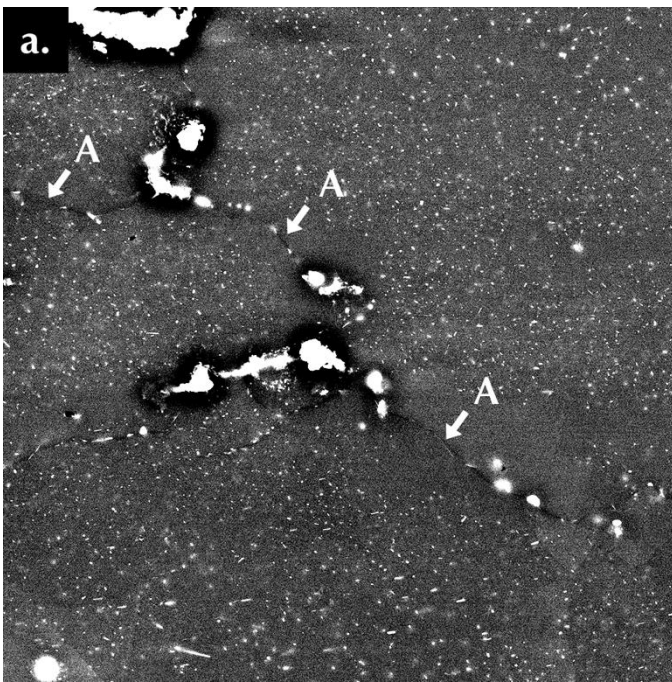


Figure 3. SEM-CBS micrographs of the 2050 alloy a. as-received state and b. after ageing where A arrows indicate grain boundaries with the presence of a precipitate free zone from either side, and B arrows are pointing towards possible sub-grains boundaries.

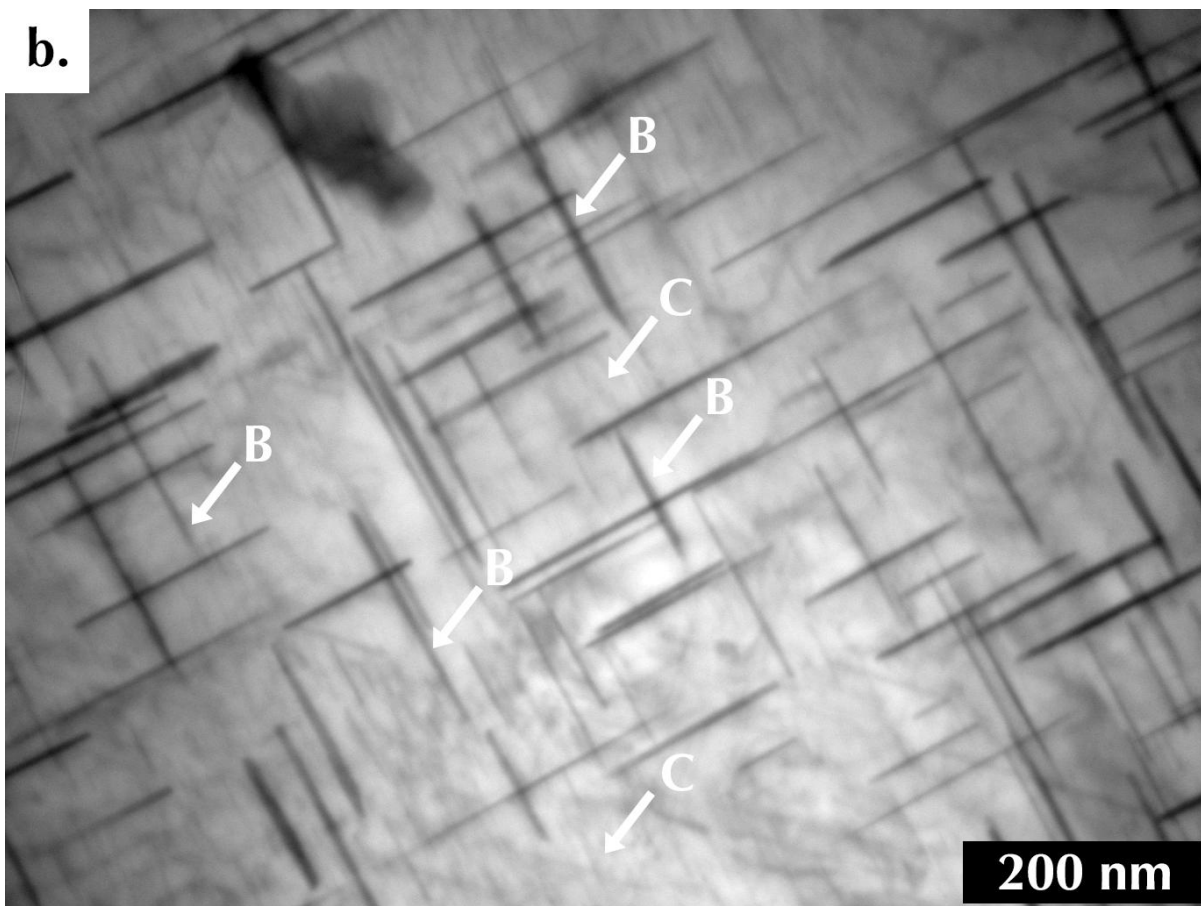
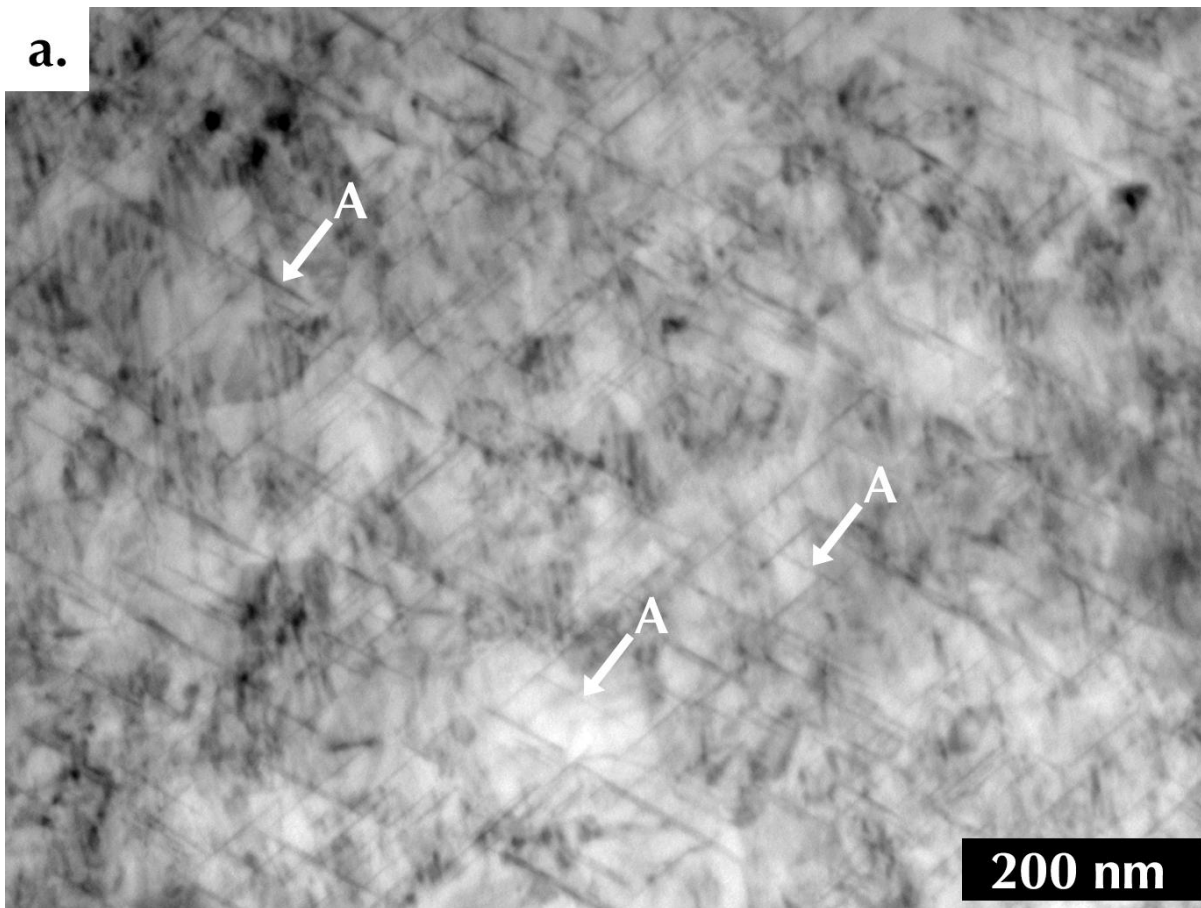


Figure 4. TEM observations on the as-received state alloys. a. The 2050 alloy observed in  $\langle 110 \rangle_{Al}$  direction and b. 2219 alloy observed in  $\langle 001 \rangle_{Al}$  direction. A arrows show precipitates in  $(111)_{Al}$  planes, B arrows the precipitates in  $(100)_{Al}$  planes and C arrows show areas with small precipitates.

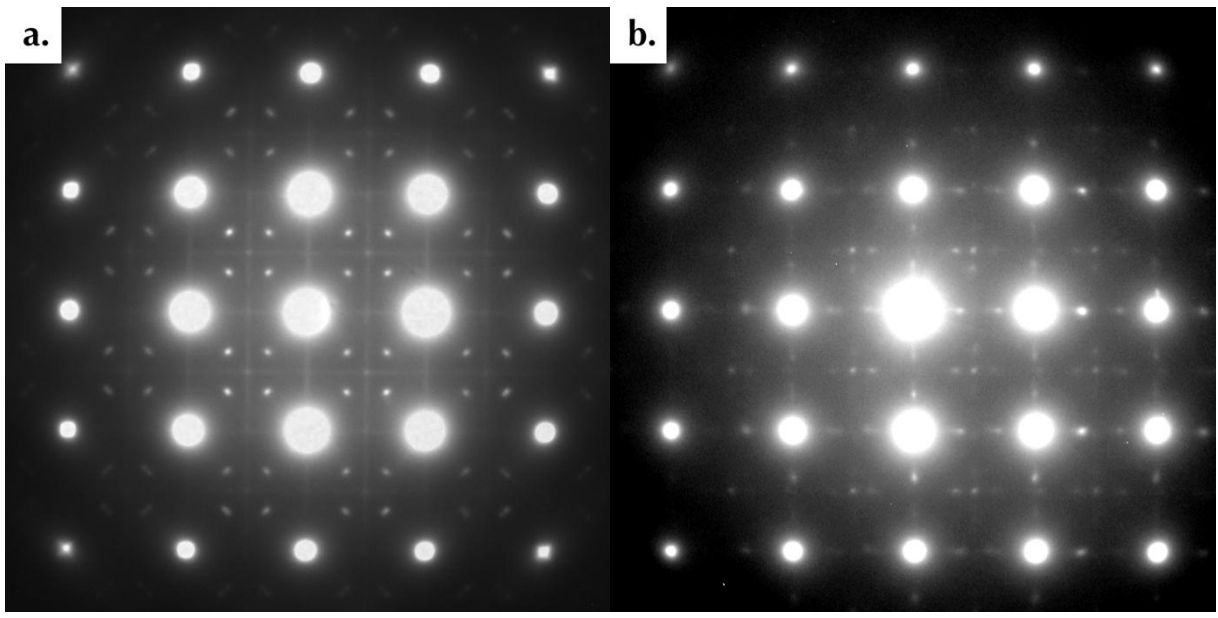


Figure 5. SAED patterns of a. the 2050-T84 and b. the 2219-T851 captured with an electron beam parallel to the  $\langle 001 \rangle_{Al}$

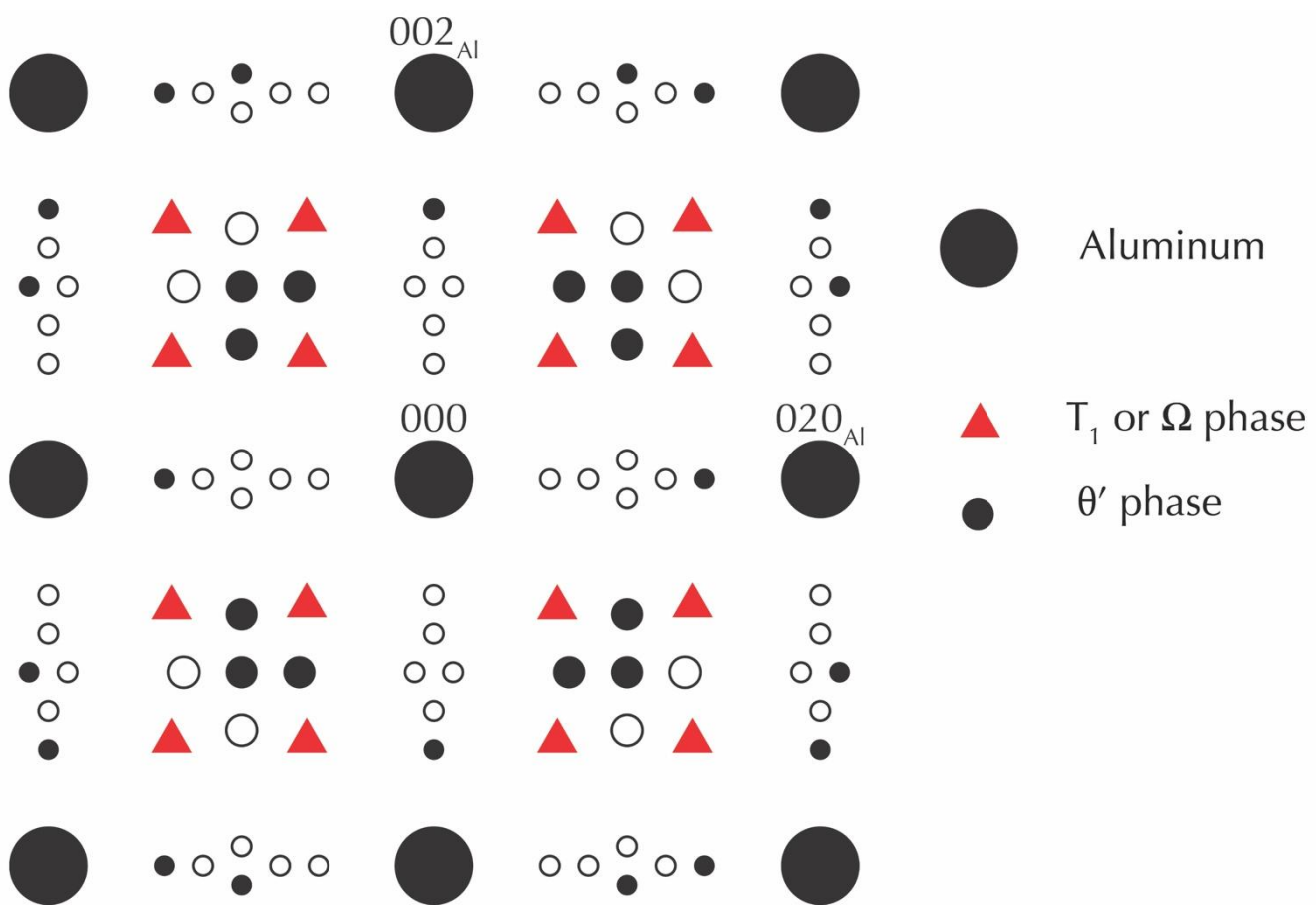


Figure 6. Schematic diffraction pattern of the direct (disks) and double diffraction (circles) of the  $\theta'$ ,  $T_1$  and  $\Omega$  phases based on the literature [42,47,48].

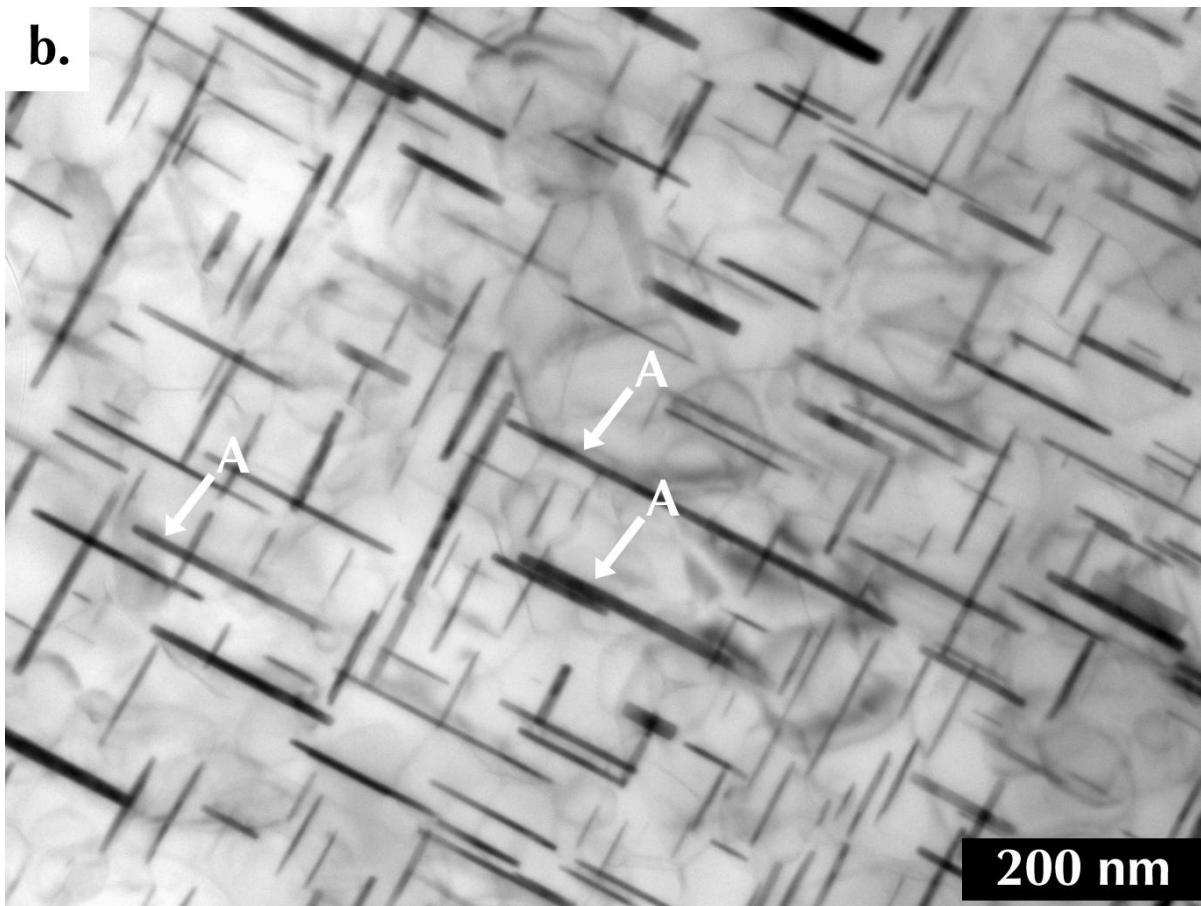
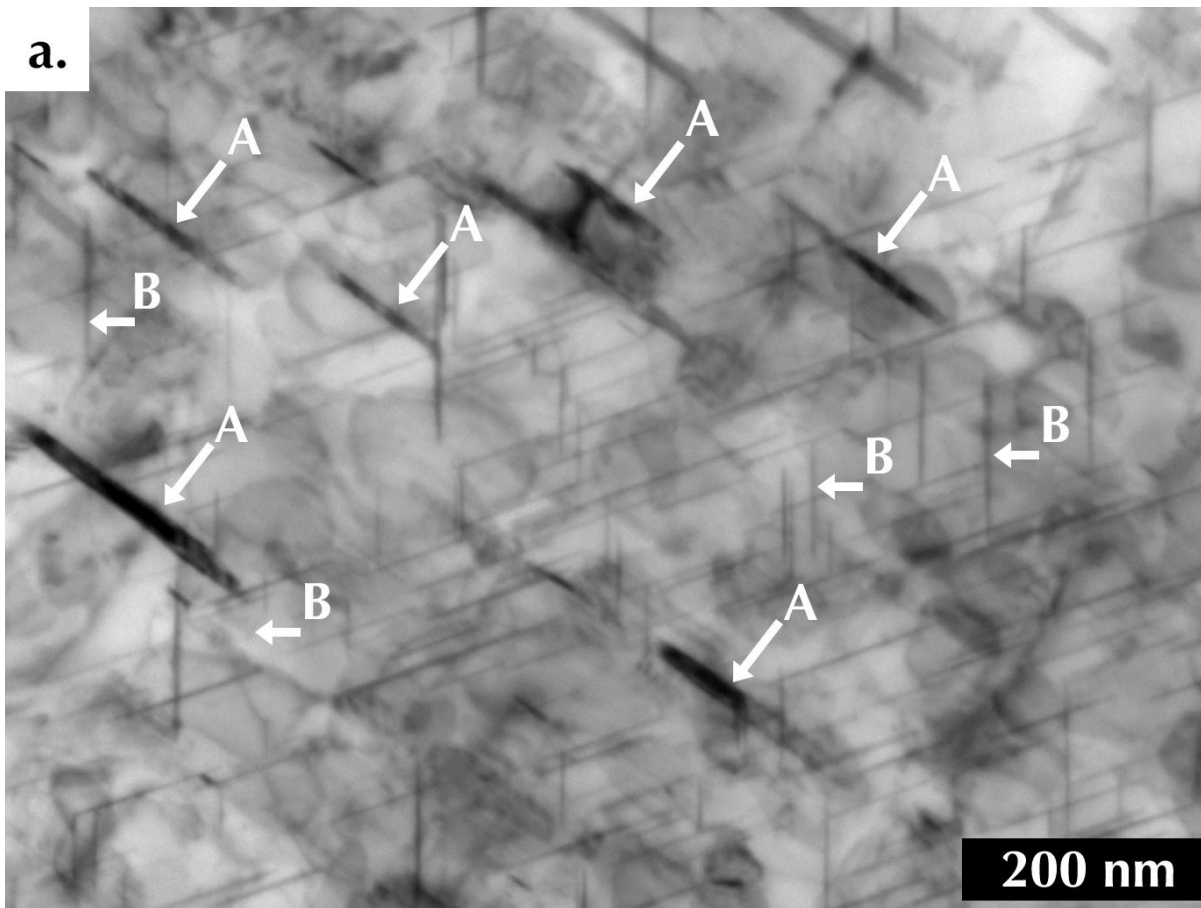


Figure 7. TEM observations of the aged alloys. a. The 2050 alloy in  $\langle 110 \rangle_{Al}$  direction and b. 2219 alloy in  $\langle 001 \rangle_{Al}$  direction. A arrows show precipitates in  $(100)_{Al}$  planes and B arrows precipitates in  $(111)_{Al}$  planes.

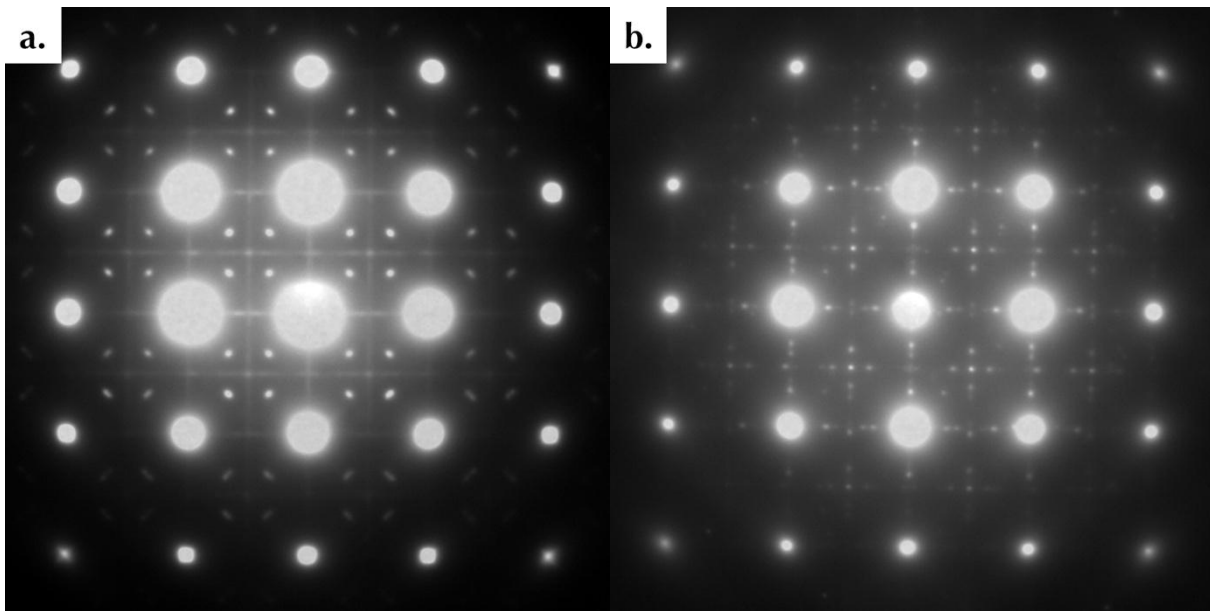


Figure 8. SAED patterns of a. the aged 2050-T84 and b. the aged 2219-T851 captured with an electron beam parallel to the  $[001]_{Al}$ .